ORIGINAL ARTICLE

Preparation of high-performance manganese-based pseudocapacitor material by using spent lithium-ion battery anode graphite via mechanochemical pretreatment

Lujie Dai[1], Bang Li[2], Jia Li[1]* and Zhenming Xu[2]

Abstract

The potential for recycling graphitic carbon from lithium-ion battery (LIB) anodes has been overlooked due to its relatively low economic value in applications. This study proposed to use graphene nanoplates (GNPs), which were obtained from spent lithium battery anode graphite, treated with ball-milling method, for hydrothermal synthesis of MnO_2-supported graphene nanoplates (MnO_2/GNPs) composites materials. The composites exhibited excellent electrochemical characterization curves, indicating ideal capacitance characteristics. The analysis of MG24-20 material showed the good impact resistance and capacity retention around 100% with capacitance of 124.6F/g at 10 mV/s, surpassed similar samples using precious metals and high-end materials, enabling the reuse of spent graphite in energy conversion and storage system for effective utility.

Keywords Spent graphite, MnO_2, Mechanochemistry, Graphene nanoplates, Electrochemistry, Hydrothermal method
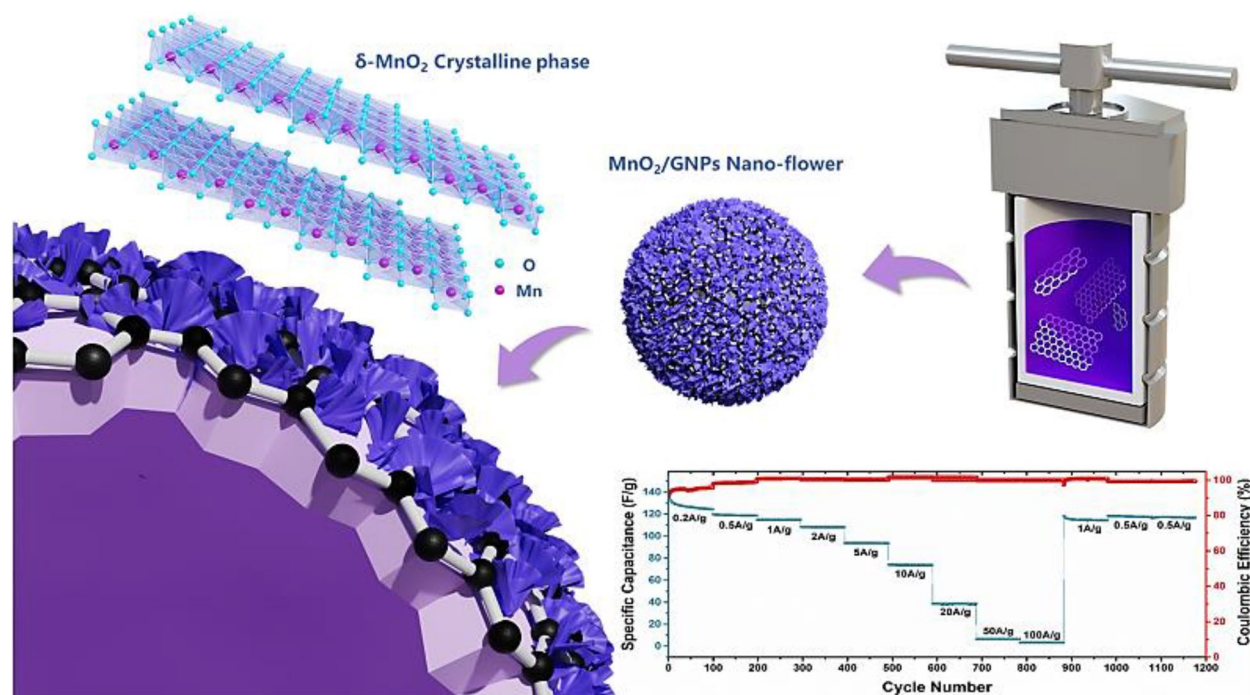
*Correspondence:
Jia Li
weee@sjtu.edu.cn
Full list of author information is available at the end of the article

Dai *et al. Carbon Neutrality*   (2024) 3:3

Page 2 of 12

Graphical Abstract

1 Synopsis

In this study, we explored a new way to recover the spent graphite of waste lithium-ion batteries with high value. It focuses on the efficient preparation of graphene materials with enhanced electrochemical capacity using one-step mechanochemical methods without the use of additives. The application and exploration of the performance of the spent graphite supercapacitor by using potassium permanganate hydrothermal loaded manganese dioxide were carried out, and its capacitance performance reached the middle reaches of the industry.

2 Introduction

Graphite is widely used in the negative electrode of lithium batteries and helps to achieve high energy storage [28]. With the increasing attention paid to battery recycling, compared with fined regeneration of heavy metal in cathode, the graphite, which has the proportion of 12%-21% from used lithium batteries, has typically not been properly recycled [19, 35]. Instead, they are often incinerated, resulting in severe pollution and producing hazardous waste like metals, binders, toxic and flammable electrolytes [15, 37]. The demand for graphite is further compounded by the projected tenfold increase in the use of lithium batteries in electronic devices over the next decade [17].

Therefore, the recycling of spent graphite in waste lithium-ion batteries is crucial to the sustainable development of the industry [8]. In the current recycling process, spent graphite is usually used as a reducing agent for high-temperature smelting transition metals [23]. However, it can be effectively recycled through multi-step process, involving pretreatment, purification, and subsequent reuse or transformation into new materials [8, 19, 21]. Natarajan et al. [20] have demonstrated that anode graphite, due to the reduction of interlayer forces during battery cycling, offers advantageous characteristics for generating premium graphene [20]. Moreover, when compared to commercial graphite, spent graphite exhibits structural defects, surface functional groups, and metal impurities that can be harnessed to synthesize and enhance the performance of graphite-based functional materials [1, 2].

The mechanochemical method, which is a simple and environmentally friendly approach for producing graphene materials, has garnered attention [10, 22, 27]. Previously, the research group discussed the preparation of graphene nanosheet materials with high specific surface area and relatively hydrophilic after dry ball milling of

Dai *et al. Carbon Neutrality*   (2024) 3:3

Page 3 of 12

waste lithium battery negative graphite [30]. The properties of the purified material applied to the double layer capacitance were experimentally analyzed. Despite its mediocre performance than activated carbon, graphene oxide and other cutting-edge materials under similar experimental conditions, it remains a promising substrate material with high specific surface area for oxide loading. Consequently, the group has shifted its focus to the preparation of composite metal oxide materials.

Compared with double-layer capacitors based on carbon materials, the transition metal oxide pseudocapacitor energy storage mechanism implies a higher energy density [3]. Manganese dioxide (MnO_2) is a resource-rich and relatively cheap transition metal oxide with excellent pseudocapacitance, which can theoretically reach 1111F/g, but the actual performance of MnO_2 is usually limited by its low conductivity [9, 25]. To address this limitation, researchers have explored the strategy of incorporating MnO_2 into materials with excellent electrical conductivity,, such as gold [13, 31], carbon nanotubes [12, 26], graphene [9, 16], etc. However, it's important to consider that the use of precious metals, like gold, can raise the production costs, and the preparation process for materials like carbon nanotubes and graphene tends to be relatively complex [24, 34].

In this study, the primary objective is to investigate the electrochemical properties of MnO_2/GNPs, where graphene materials were first prepared through ball milling and subsequently subjected to a hydrothermal process with potassium permanganate, intended for use as electrode materials in water-based electrochemical capacitors. The research also delves into a comprehensive analysis of how various electrochemical conditions impact the capacitance behavior, with the ultimate goal of achieving higher capacitance in manganese-based electrodes.

3 Experimental

3.1 Preparation of GNPs

The spent graphite was obtained by disassembling used lithium-ion battery. The battery was fully discharged in a 10% sodium chloride solution for 24 h. The positive electrode, diaphragm, and coil were removed, leaving a copper foil with graphite, which was then scraped to obtain graphite powder. The powder was soaked in deionized water for 24 h, filtered, and vacuum dried. Pyrolysis in a tube furnace at 100 mL/min for 2 h removed the binder and organic components, resulting in the obtained spent graphite sample named SG. 60g of stainless-steel beads to fabricate the GNP, dry grinding at 20Hz for 24 h. To remove residual impurities, the prepared GNPs powder (0.5g) was mixed with 100ml 1.0M hydrochloric acid solution, stirred for 24 h, filtered, washed, and dried

at 80°C for 12 h. The resulting pure milled GNPs were named MG24.

3.2 Preparation of MnO₂/GNPs composites

The MnO_2/GNPs composites were synthesized using a hydrothermal method. In a 50 mL Teflon-lined stainless-steel autoclave, 20 mg of MG24 was added, followed by the addition of 30 mL of potassium permanganate solution with varying concentrations (0, 5, 10, 15, 20, 30 mmol/L). The reaction took place at 150 °C for 4 h. After the autoclave naturally cooled down, the remaining potassium permanganate was removed by repeatedly rinsing the sample with deionized water using centrifugation. The resulting residue was then dried at 60 °C for 12 h. It was finely ground using a quartz mortar and named based on the concentration of potassium permanganate solution used, such as MG24-0, MG24-5, MG24-10, MG24-15, MG24-20, MG24-30, respectively (Fig. 1).

3.3 Preparation of GNPs working electrode

For the preparation of the working electrode, prepared electrochemical active material MnO_2/GNPs were mixed with PTFE(Polytetrafluoroethylene), acetylene black at weight ratio of 9:0.5:0.5, blending in diluted ethanol solution under ultrasound. The resulting mixture was rolled, cut into 1×1 cm^2 slice, pressed onto nickel foam under 20 MPa, and dried at 60 °C for 12 h. The mass loading of each electrode was about 1.0 mg/cm^2.

3.4 Characterization methods

X-ray diffraction (XRD) analysis was performed using a Mini Flex 600 XRD instrument from Japan, covered the 2θ range of 5–90° at 5° min^{-1}. Raman spectra were obtained using a Renishaw inVia Qontor Raman spectrometer from England, conducted in the range of 100–3500 cm^{-1}. X-ray photoelectron spectra (XPS) were acquired using an AXIS UltraDLD XPS instrument to identify the chemical components present in the sample. Scanning electron microscopy (SEM) images were captured using a GAIA3 FIB-SEM double beam electron microscopy system, while SEM images with energy-dispersive X-ray spectra (EDS) mappings of MnO_2/GNPs were obtained using a JEOL-2100F/F200 instrument.

3.5 Electrochemical measurements

All electrochemical experiments were conducted using a CS2350H electrochemical workstation in a standard three-electrode setup. The prepared MnO_2/GNPs working electrodes, a platinum foil as the counter electrode, and a saturated calomel electrode (SCE) as the reference electrode, performing in 1M Na_2SO_4 aqueous electrolyte solution. Electrochemical characterizations were performed by cyclic voltammetry (CV), galvanostatic
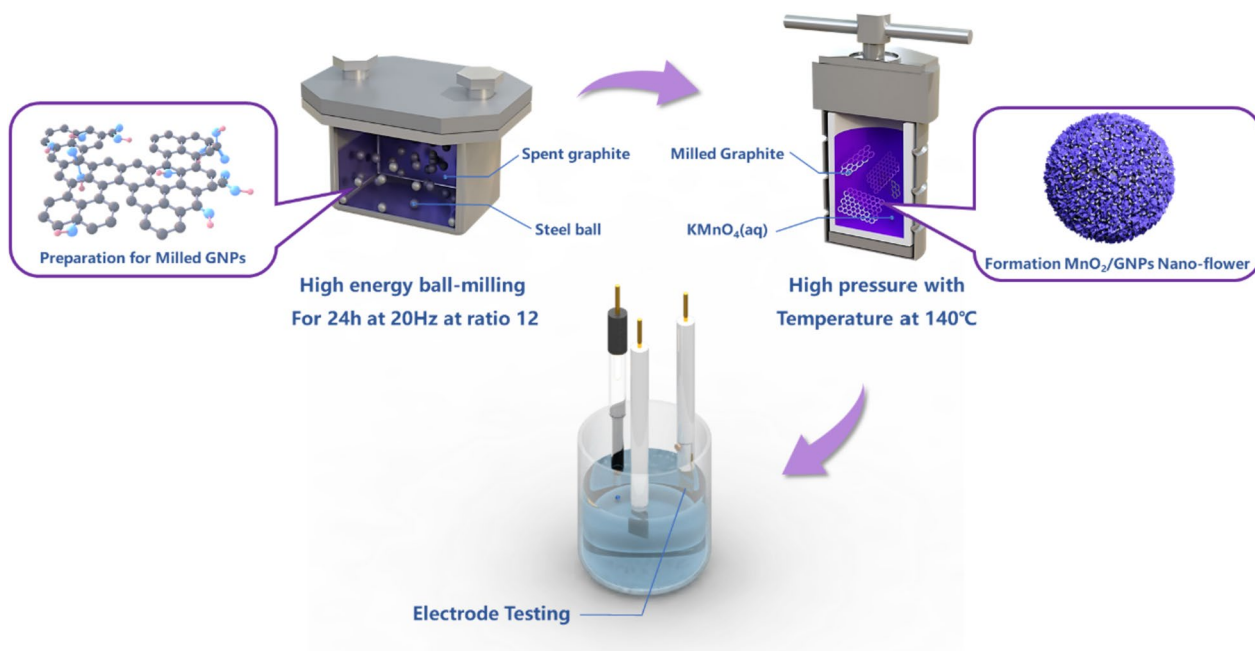
Fig. 1 Experiment processing flow chart of MnO_2/GNPs composites

charge/discharge (GCD), cycling performance, and electrochemical impedance spectroscopy (EIS).

The specific capacitance (C_s) values of the electrode can be calculated using obtained curves of CV and GCD in following equations

$$C_s = \frac{1}{mv\Delta V}\int I dV$$

$$C_s = \frac{I\Delta t}{m\Delta V}$$

where I is the discharge current (A), v is the scan rate (V/s), Δt is the discharge time (s), m is the mass of active material in the working electrode (g), and ΔV is the potential window (V).

4　Results

4.1　Structure characterization of MnO_2/GNPs

MnO_2 has many crystal forms as α, β, δ, γ, and its crystal structure has a certain correlation with the electrochemical performance [5, 7]. As shown in Fig. 2, there are two different types of MnO_2 crystals, each of which has an octahedral composition of manganese oxide (MnO_6). The two different crystal types have a 2 × 2 channel for ion migration, with a size of about 4.6 × 4.6 Å for the Cryptomelane type, as α-MnO_2, and a layered composition with ion migration in between the layers for the Birnessite as δ-MnO_2, which the layer separation is roughly 7.14 Å. Gupta et al. synthesized MnO_2 nanostructures with different crystal types, found that the activity per unit of electrochemical surface area was
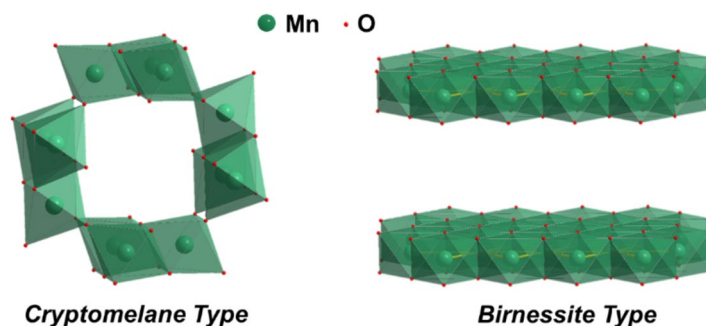

Fig. 2 Schematic diagram of crystalline structure for Cryptomelane and Birnessite MnO_2

δ-MnO_2 > α-MnO_2, indicating the better crystal type in electrochemical application [6].

The phase and crystal structure of materials were analyzed at different $KMnO_4$ solution concentrations using X-ray diffraction. The results, shown in Fig. 3a, reveal a stronger graphite peak for MG24 compared to Mg24-5. The emergence of new phase peaks matching MnO_2, specifically the Cryptomelane type, is observed at 2-Theta degrees 12.8°, 18.1°, 29°, 37.5°, 42°, and 60.3°. As the solution concentration increases from 5 to 15 mmol/L (Fig. 3b), the graphite peak diminishes, while the prepared MnO_2 retains the Cryptomelane type. At concentrations of 20 mmol/L or higher (Fig. 3c), the MnO_2 phase peak shifts to a lower angle, and diffraction peaks at 2-Theta degrees 18.1°, 42°, and 60.3° disappear, indicating a different crystal type, identified as Birnessite based on database searches and literature comparisons. The strength of the graphite (002) crystal surface peak decreases with increasing $KMnO_4$ concentration (Fig. 3c), likely due to the higher crystallinity and stronger diffraction peaks of the generated MnO_2 masking the graphite peak. Additionally, the hydrothermal synthesis process leads to the consumption of graphite in the reaction, causing a gradual decline in the graphite peak as the concentration rises, as shown in Table S1.
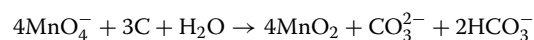
$$4MnO_4^- + 3C + H_2O \rightarrow 4MnO_2 + CO_3^{2-} + 2HCO_3^-$$

Figure 3d presents the Raman spectra analysis results of the materials produced with varying $KMnO_4$ concentrations. In the experimental group with $KMnO_4$, the graphitized G peak at 1580 cm^{-1}, D peak at 1350 cm^{-1} and 2D peak at 2700 cm^{-1} weakened and the degree of weakening increased with concentration, comparing to MG24. At concentration 20 mmol or more, the D and 2D peaks nearly disappeared, while the G peak showed only a small peak. In addition, the introduction of $KMnO_4$ resulted in the appearance of characteristic MnO_2 peaks between 600 and 700 cm-1 wavenumbers. These results demonstrate the existence of the reaction process described in the hydrothermal process, through which different crystalline MnO_2-supported graphene nanosheet materials are prepared at different concentrations.

SEM and TEM were used to further examine the microscopic morphology and crystal structure of MG24-5 and MG24-20, respectively, which were loaded with various crystalline forms of MnO_2. Figure 4 displays SEM images of the minerals MG24-5 and MG24-20. A significant number of microscopic particles can be seen on the surface of large particles in the MG24-5 sample, and nano-rod-like crystals can be seen to protrude from
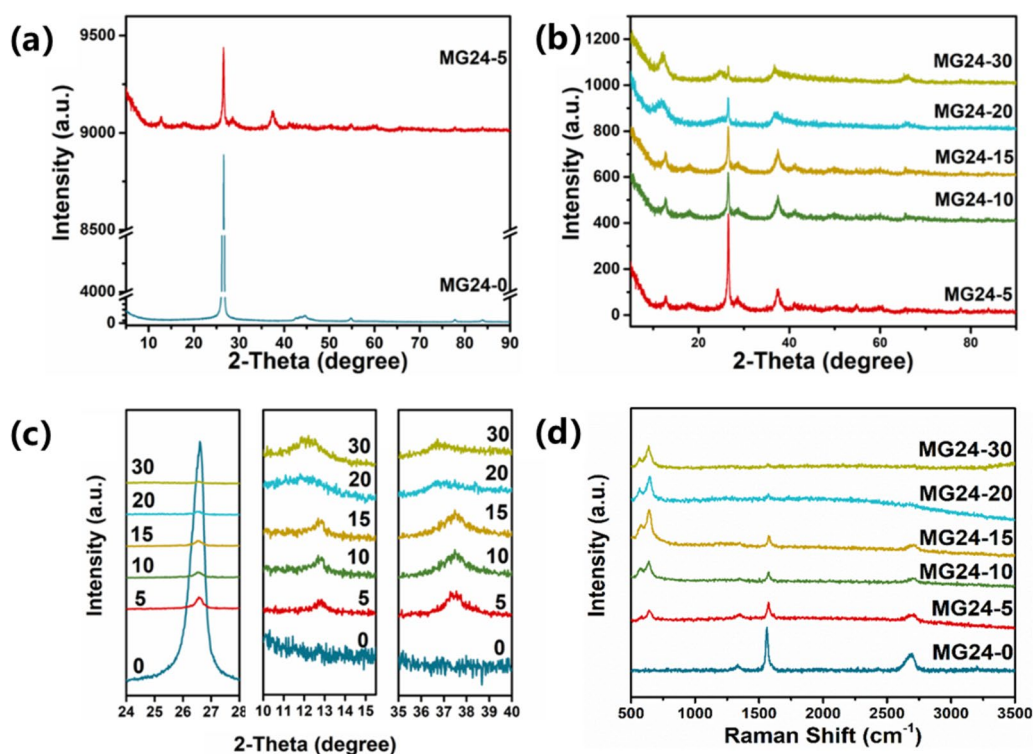

Fig. 3 **a**–**c** XRD pattern of MnO_2/GNPs synthesized at different $KMnO_4$ concentration. (Noted as MG24-n, n refers to the solution concentration, mmol/L); **d** Raman spectra of different MnO_2/GNPs

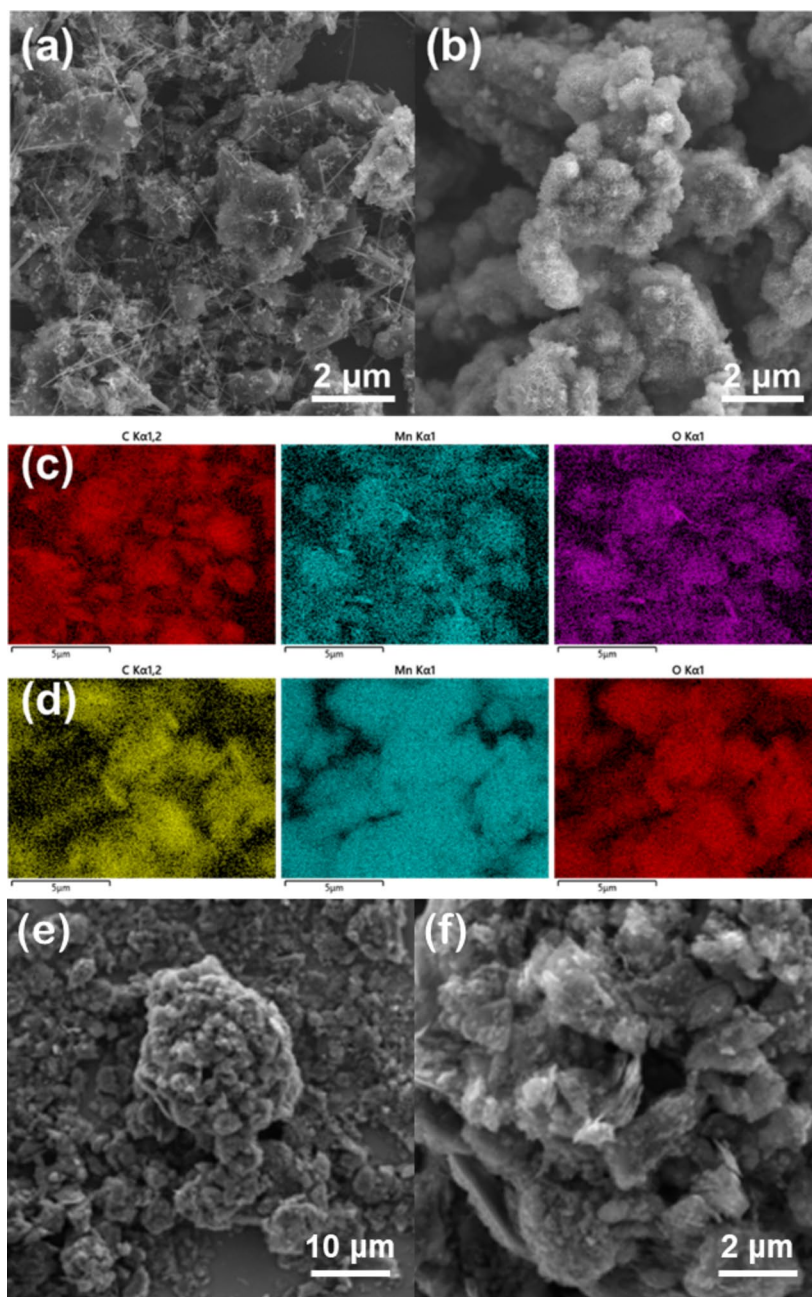Dai *et al. Carbon Neutrality*   (2024) 3:3

Page 6 of 12

Fig. 4 SEM observation of **a** MG24-5, **b** MG24-20 and Elemental EDS mapping **c** MG24-5, **d** MG24-20, **e**–**f** MG24-0

large particles. According to the two-dimensional properties of Birnessite, MG24-20 depicts a cluster of flowers. This material's surface is noticeably rougher and has more pore structure because to the cluster petal structure. The MnO_2 was consistently produced on the surface of GNPs, according to the EDS data, while MG24-20 clearly generated a thicker MnO_2 supported layer. These findings are best understood when compared to MG24-0 as seen in Fig. 4(e-f), where the nanorod-like and

cluster-like petal structures are grown based on the flake graphite and many tiny plates between 0.1 and 2 μm in size of MG24-0.

Figure 5a shows the TEM observation of MG24-5, revealing a thin layer of graphene serving as the substrate, with the development of surface flake and nanorod-like crystals in zones 1 and 2, respectively. High-resolution TEM images show clear diffraction fringes in region 1 spacing of 6.92 Å corresponding to the Cryptomelane
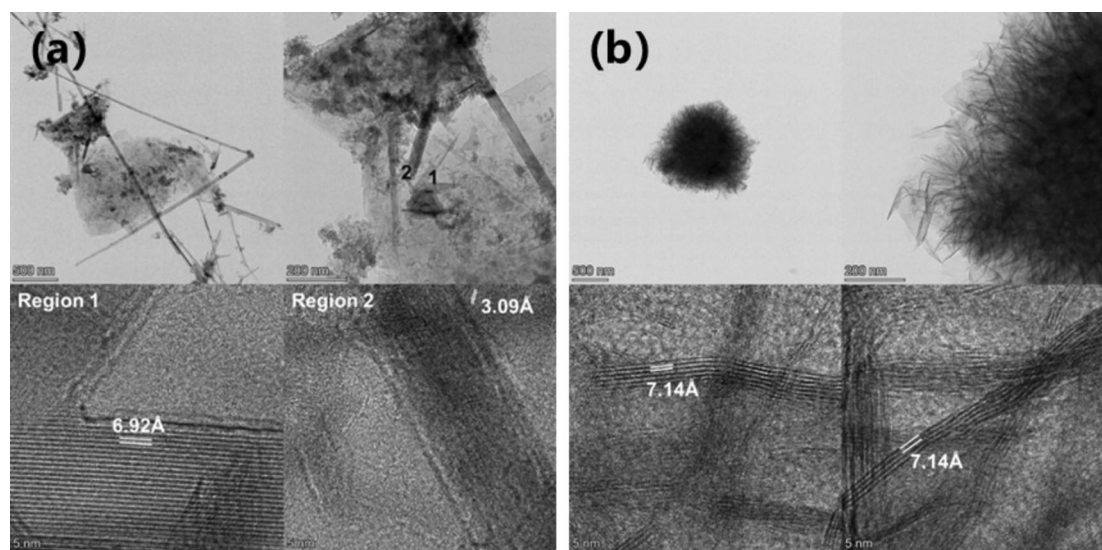
Fig. 5 TEM observation of **a** MG24-5, **b** MG24-20

(110) crystal face, and the measured crystal face spacing of 3.09 Å in region 2 matches the Cryptomelane (310) crystal face, validating the XRD analysis. Notably, the diffraction fringes of the thin graphene layer are not directly observed, possibly due to the destruction of the graphite crystal structure caused by $KMnO_4$ etching during the hydrothermal reaction. Figure 5b shows the TEM image of MG24-20 material, presented as displays MG24-20 material as petal-shaped nanosheet aggregates. Particle size differs significantly from MG24-5, likely due to severe $KMnO_4$ etching. Limited by TEM observation, only the nanosheets growing outside the petal-like particles were observed and analyzed. According to the high-resolution TEM images, the measured diffraction fringe spacing is 7.14 Å, which corresponds to the (001) crystal plane of Birnessite type. Few diffraction fringes indicate thinner layered MnO_2 nanosheets with about $5 \sim 10$ layers. Similarly, the characteristics of graphene nanosheet materials could not be directly observed due to continuously growth of thin sheet MnO_2 on the surface of GNP particles, forming a thick shell layer.

4.2 Chemical properties of MnO_2/GNPs

Using the thermogravimetric method, the element composition of MnO_2/GNP materials prepared at different concentrations was quantitatively analyzed. The results are shown in Fig. 6 and Table 1. The weight loss curves of all materials exhibit in two stages: the removal of bound water in the first stage and the reaction reduction of MnO_2 with graphite and air resulting in Mn_2O_3, in the second stage. Higher concentrations mean larger loads of MnO_2. It can be noted that MG24-20 and MG24-30 with

two-dimensional characteristics have relatively more structural water, facilitating ion migration. The molar ratio of C to Mn remains unchanged at low concentrations, with the addition of $KMnO_4$, a specific amount causes partial consumption of graphite. This indicates the distinct growth modes of MnO_2 under different concentrations. The one with relatively lower concentration is likely heat-induced breakdown of $KMnO_4$ followed by nucleation crystallization, while the latter involves etching reactions, leading to MnO_2 with different crystal structures.

XPS was used to analyze the chemical states of elements on the surface of MG24-20 material, and the results are shown in Fig. 7. The full spectrum shows that MG24-0 surface only contains C and a small amount of O elements, MG24-20 surface elements also contain Mn and a small amount of K. Compared with MG24-0, the peak of C1s on MG24-20 is significantly decreased, while the peak of O1s is significantly increased. Comparing the C1s spectra of the two groups of materials (Fig. 7b), it can be seen that the surface C of MG24-20 is mainly composed of oxygen-containing functional groups and sp2 hybrid carbon atoms, which also proves the oxidation etching of graphite materials by potassium permanganate. Figure 7c shows the O1s spectrum of MG24-20, which can be divided into two groups of 529.9 eV and 531.9 eV peaks, corresponding to Mn–O-Mn bond in Mangano-oxygen octahedron and Mn-OH bond on Mangano-oxygen hydrate, respectively, proving the existence of manganese oxides and the presence of structural water is also conducive to the migration and diffusion of electrolyte ions [33]. The Mn3s
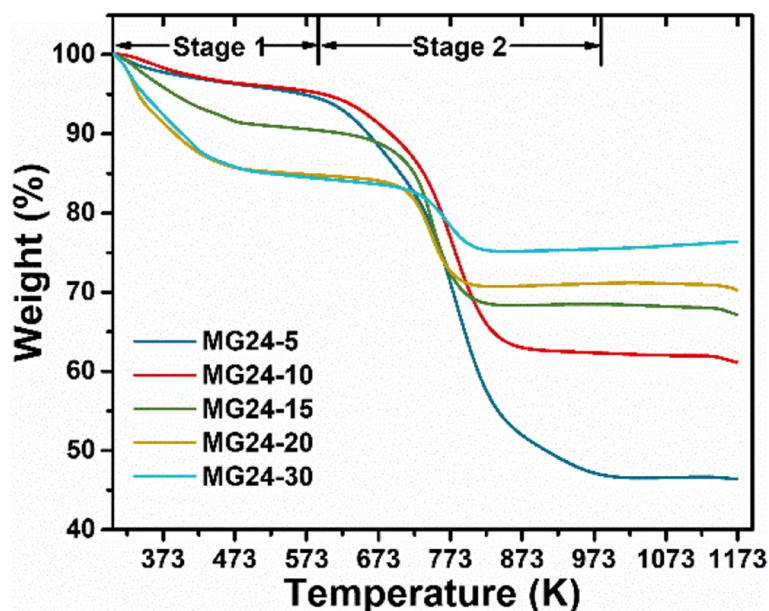
Fig. 6 TG curves at 20 K/min in air for MnO$_2$/GNPs

Table 1 Component fraction in MnO$_2$/GNPs calculated based on TG curves

Sample	Component (wt.%)			MnO$_2$·nH$_2$O	C\Mn Mole Ratio	
	GNP	MnO$_2$	H$_2$O	n	Before reaction	After reaction
MG24-5	58.11	35.78	6.11	0.82	11.11	11.77
MG24-10	40.03	52.38	7.59	0.70	5.56	5.54
MG24-15	26.26	59.96	13.79	1.11	3.70	3.17
MG24-20	14.15	63.49	22.36	1.70	2.78	1.61
MG24-30	6.93	69.39	23.68	1.65	1.85	0.72

spectrum in Fig. 7d shows two peaks, between which the energy separation can be used to determine the manganese valence. Energy separation of 4.84 eV indicates Mn^{4+} ions to be dominated [14], supporting the conjecture of the formation of MnO$_2$.

4.3 Pseudocapacity of MnO$_2$/GNPs

Different MnO$_2$/GNP electrodes were tested in a three-electrode electrolytic cell. Figure 8a shows the CV curves of each material at a scanning speed of 50 mV/s. MG24-0 exhibited low current response, which increased significantly after loading MnO$_2$, along with increased capacitance. MG24-0 relied on double layer capacitance electrostatic adsorption, with a specific capacitance of 16.1F/g at this scanning speed. MnO$_2$/GNP electrode demonstrated Faraday reaction with Na$^+$ ions in the electrolyte:

$$MnO_2 + Na^+ + e^- \leftrightarrow MnOONa$$
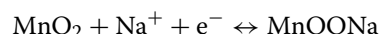
MnO$_2$ undergoes reversible REDOX reaction of Mn^{4+}/Mn^{3+}, with Na$^+$ ions' adsorption on the surface or embedding through channels in the lattice. This enables the MnO$_2$/GNP electrode to exhibit higher specific capacitance, which increases with larger loads. At 50 mV/s, CV current response decreases for MG24-30, possibly due to excessive MnO$_2$ thickness hindering ion diffusion and migration. All MnO$_2$/GNP electrodes exhibit ideal rectangular CV curves, indicating good capacitance behavior.

Specific capacitance changes were calculated for different MnO$_2$/GNP electrodes at various scanning speeds in Fig. 8b. Increasing specific capacitance exhibited with MnO$_2$ loading increasing under lower scan speeds, due to the effective ion migration and diffusion on the
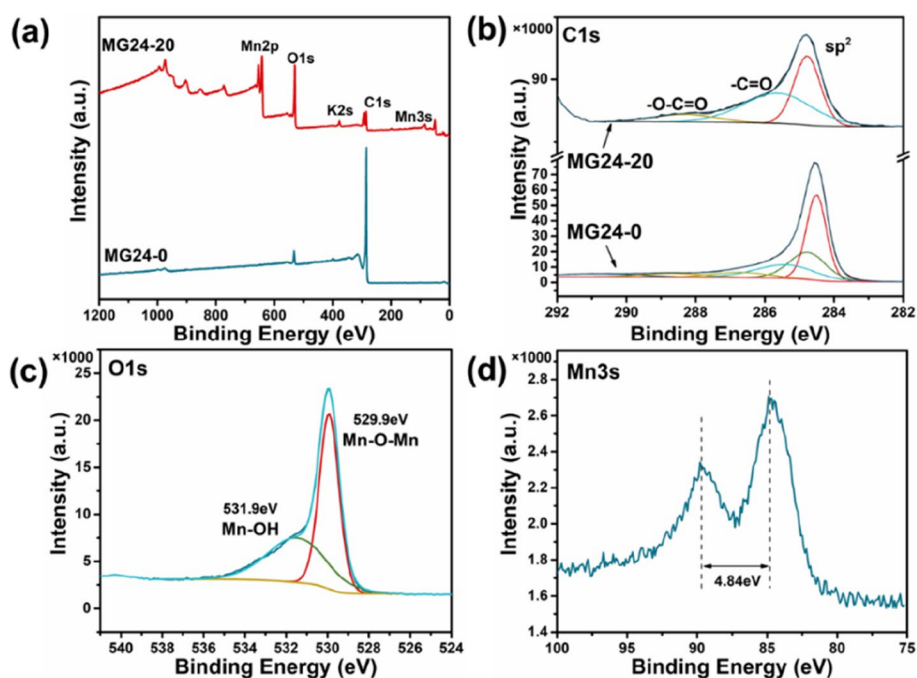
Fig. 7 **a** Full spectrum of XPS, and high resolution XPS spectrum of **b** C1s, **c** O1s, **d** Mn3s

electrode's surface and within its crystal structure. When increasing the scanning speed from 5 mV/s to 100 mV/s, it led to decreased specific capacitance due to mass transfer limitations. MG24-30 showed the most significant decay, potentially caused by its thicker MnO_2 surface impeding ion transport.

The specific capacitance values provide insights into the impact of different MnO_2 crystal structures. MG24-5, 10, and 15 (Cryptomelane type) showed a linear relationship between specific capacitance and MnO_2 loading. MG24-20 and 30 (Birnessite type) exhibited a significant capacitance increase, particularly from MG24-15 to MG24-20. Cryptomelane structures feature 2D particles on graphene nanosheets and 1D nanorods with 1D channel of 4.6×4.6 Å for ion migration. Birnessite type type is petal-like cluster 2D sheet, with ions diffusing into the crystal transported in two dimensions between the crystal faces with a spacing of 7.14 Å. Birnessite structures of MG24-20 petal-like cluster structure implies a possible larger surface area, greater roughness, and more pore structure [4], contributing to its high specific capacitance.

EIS analysis of MG24-0, MG24-5, and MG24-20 in Fig. 8c revealed their electrochemical characteristics. MG24-0 exhibited double-layer capacitor behavior, while MnO_2-loaded samples showed a complete semicircle in the high-frequency region. The circle's radius increased with higher loading, indicating increased charge transfer resistance. MG24-20's relatively thick outer layer of MnO_2 on graphene nanosheets hindered charge transfer.

However, in the low-frequency region, MG24-20 showed a smaller slope, indicating lower ion transfer resistance. This can be attributed to the different MnO_2 crystalline types and the more structured water in MG24-20, facilitating ion diffusion and migration.

MG24-20 exhibited higher capacitance and minimal capacity loss at high scan rates. Its constant GCD characteristics were analyzed in Fig. 8d. The GCD curves of MG24-20 electrodes between 0.2A/g and 10A/g showed symmetric triangles across current densities, indicating ideal capacitive behavior. The electrode had a voltage drop of only 0.025 V at 1A/g.

The electrode's cycling performance was evaluated in a three-electrode system using the GCD method in Fig. 8e. It underwent 100 charge−discharge cycles at various current densities. At 0.2A/g, the electrode's initial capacity was 136.16 F/g, retaining 91.38% capacity after 100 cycles, with increased Coulomb efficiency from 91.44% to 95.8%. At 0.5A/g, the initial specific capacitance was 119.90 F/g, with only a 0.82% loss after 100 cycles. At 10A/g, specific capacitance decreased, but cycle retention rate remained close to 100% with high Coulomb efficiency, indicating reversible surface Faraday reaction. Beyond 10A/g, the electrode suffered impractical capacity loss. However, it still exhibited near-perfect Coulomb efficiency at high current densities. At low current densities, the electrode recovered its initial capacity and showed stable cycling with around 100% capacity retention. Initial specific capacitance was 118.43 F/g, while at
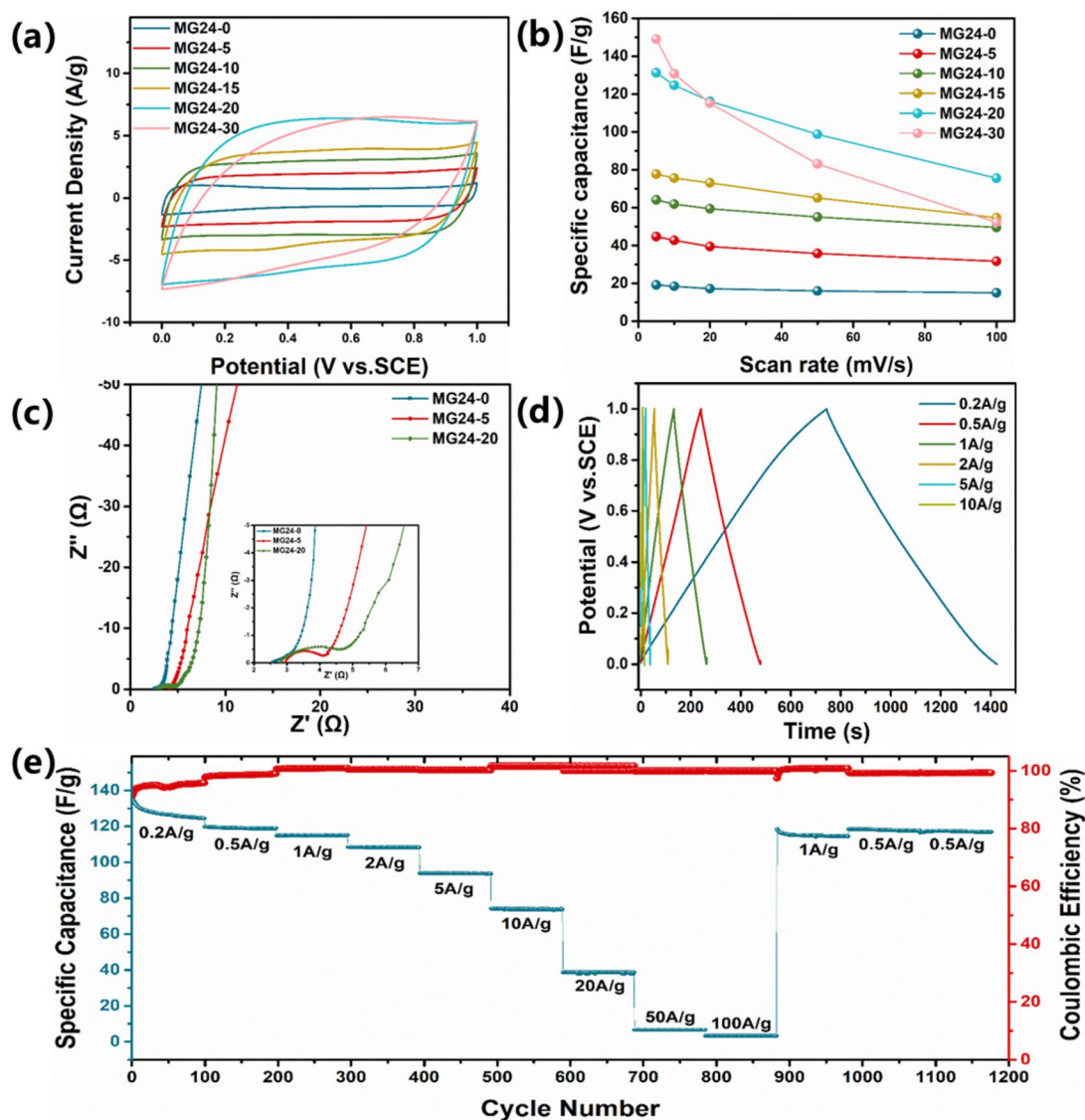
Fig. 8 **a** CV curves for different MnO$_2$/GNP material recorded in a three electrode cell, 1.0 M Na2SO4 is applied as electrolyte, potential window in 0~1 V, Saturated calomel electrode (SCE) as reference; **b** Specific capacitance of different MnO$_2$/GNPs under different scan rate; **c** Nynquist plot for different MnO$_2$/GNPs; **d** GCD curves for MG24-20 material at different current density; **e** Cycling stability and columbic efficiency of MG24-20 at different current density

the end of the cycle, it was 116.81 F/g. These results demonstrate the MG24-20 electrode's exceptional resistance to current shocks and cycling stability.

Table 2 presents summary of capacitive properties for carbon/manganese dioxide composites found in published literature. These methods typically involve complex chemical synthesis under harsh synthesis conditions. In contrast, this paper introduces a simpler and efficient two-step synthesis approach using mechanical ball milling and hydrothermal reaction with low-cost waste graphite. The performance of this material is comparable to composites synthesized using expensive graphene and

carbon nanotubes, showcasing the valuable utilization of waste graphite. It should be noted that this study focused on MG24 as the carbon substrate, limiting the material's potential. Further exploration of different ball milling parameters can enhance the composite's performance in the future.

5 Conclusion

The article introduced a simple and efficient method to convert waste graphite into MnO2/GNP composites, synthesizing via hydrothermal conditions using mechanochemical-pretreated GNP materials. The analysis

Dai *et al. Carbon Neutrality*   (2024) 3:3

Page 11 of 12

Table 2 Comparison of electrochemical capacitor performance of MnO_2/C composites in published work and this work

Sample	Preparation method	Electrolyte	Scan Rate/ Current density	Specific Capacitance (F/g)	Ref
3D Graphene/MnO_2	CVD on Ni foam + Electrodeposition	0.5 M Na_2SO_4	2 mV/s	130	[9]
MnO_2/GNP	Chemical exfoliation + hydrothermal reaction	2.0 M $(NH_4)_2SO_4$	10 mV/s	158	[29]
CNT/MnO_2	Chemical etching and deposition	2.0 M KCl	20 mV/s	144	[12]
Mesoporous carbon hollow sphere/ MnO_2	Templated synthesis of MCHS + Carbonization + Hydrothermal reaction	1.0 M Na_2SO_4	0.1 A/g	116.4	[36]
3D MnO_2@GCs @MnO_2	CVD on ZnO + Microwave decomposition	1.0 M Na_2SO_4	0.5A/g	265.1	[11]
3D MnO_2/Graphene hydrogel	Hummers method + hydrothermal reaction	1.0 M Na_2SO_4	1A/g	200.6	[18]
3D Graphene aerogel/MnO_2	Hummers method + 3D printing + Annealing + Electrodeposition	3.0 M LiCl	0.02A/g	212.5	[32]
MnO_2/GNP	Mechanical ball milling + Hydrothermal reaction	1.0 M Na_2SO_4	10 mV/s or 0.2A/g	124.6/136.16	This work

focused on the crystal structure of MnO_2 obtained under different conditions and the principles of hydrothermal synthesis. The capacitance of the composites was assessed through CV, GCD, and EIS, yielding a capacitance value of 136.16 F/g under 0.2A/g current density. These composites exhibited specific capacitance values comparable to carbon/manganese dioxide composites prepared using expensive graphene or carbon nanotubes and complex chemical synthesis processes. This approach enables the valuable utilization of waste graphite. Future exploration of different ball milling parameters could further enhance the composite's performance.

Abbreviations
LIB	Lithium Ion Battery
GNPs	Graphene Nanoplates
MnO_2	Manganese dioxide
MnO_2/GNPs	MnO_2-supported graphene nanoplates
SG	Spent Graphite
SCE	Saturated Calomel Electrode
CV	Cyclic Voltammetry
GCD	Galvanostatic Charge Discharge
EIS	Electrochemical Impedance Spectroscopy
C_s	Specific Capacitance

Supplementary Information
The online version contains supplementary material available at https://doi.org/10.1007/s43979-023-00079-z.

Additional file 1: Figure S1. The pretreatment to obtain graphite precursor from spent lithium-ion batteries. **Figure S2.** The illustration of ball milling effects on graphite. **Figure S3.** Analogical grinding model of MG-24 during ball milling. **Figure S4.** SEM images of (a) SG; (b-c) MG24. **Table S1.** MG24 content before/after hydrothermal treatment.

Authors' contributions
LJD: Methodology, Investigation, Experiment Design, Data Analysis, Diagramming, Writing Original Draft. BL: Experiment Validation, Diagramming. JL: Conceptualization, Writing- Reviewing and Editing, Supervision, Project administration. ZMX: Project administration, Funding acquisition.

Availability of data and materials
The datasets used and analyzed during the current study are available from the corresponding author on reasonable request.

Declarations

Ethics approval and consent to participate
Not applicable.

Consent for publication
Not applicable.

Author details
[1]China-UK Low Carbon College, Shanghai Jiao Tong University, 3 Yinlian Road, Shanghai 201306, People's Republic of China. [2]School of Environmental Science and Engineering, Shanghai Jiao Tong University, 800 Dongchuan Road, Shanghai 200240, People's Republic of China.

Dai *et al. Carbon Neutrality*   (2024) 3:3

Page 12 of 12

References

1. Anh Nguyen TH, Oh SY (2021) Anode carbonaceous material recovered from spent lithium-ion batteries in electric vehicles for environmental application. Waste Manage 120:755–761. https://doi.org/10.1016/j.wasman.2020.10.044
2. Arshad F, Li L, Amin K, Fan E, Manurkar N, Ahmad A, Yang J, Wu F, Chen R (2020) A comprehensive review of the advancement in recycling the anode and electrolyte from spent lithium ion batteries. ACS Sustainable Chem Eng 8:13527–13554. https://doi.org/10.1021/acssuschemeng.0c04940
3. Augustyn V, Simon P, Dunn B (2014) Pseudocapacitive oxide materials for high-rate electrochemical energy storage. Energy Environ Sci 7:1597. https://doi.org/10.1039/c3ee44164d
4. Ghodbane O, Pascal J-L, Favier F (2009) Microstructural effects on charge-storage properties in MnO_2-based electrochemical supercapacitors. ACS Appl Mater Interfaces 1:1130–1139. https://doi.org/10.1021/am900094e
5. Guo C, Zhou Q, Liu H, Tian S, Chen B, Zhao J, Li J (2019) A case study of β- and δ-MnO_2 with different crystallographic forms on ion-storage in rechargeable aqueous zinc ion battery. Electrochim Acta 324:134867. https://doi.org/10.1016/j.electacta.2019.134867
6. Gupta PK, Bhandari A, Saha S, Bhattacharya J, Pala RGS (2019) Modulating oxygen evolution reactivity in MnO_2 through polymorphic engineering. J Phys Chem C 123:22345–22357. https://doi.org/10.1021/acs.jpcc.9b05823
7. Hang Y, Zhang C, Luo X, Xie Y, Xin S, Li Y, Zhang D, Goodenough JB (2018) α-MnO_2 nanorods supported on porous graphitic carbon nitride as efficient electrocatalysts for lithium-air batteries. J Power Sources 392:15–22. https://doi.org/10.1016/j.jpowsour.2018.04.078
8. He K, Zhang Z-Y, Zhang F-S (2021) Synthesis of graphene and recovery of lithium from lithiated graphite of spent Li-ion battery. Waste Manage 124:283–292. https://doi.org/10.1016/j.wasman.2021.01.017
9. He Y, Chen W, Li X, Zhang Z, Fu J, Zhao C, Xie E (2013) Freestanding three-dimensional graphene/MnO_2 composite networks as ultralight and flexible supercapacitor electrodes. ACS Nano 7:174–182. https://doi.org/10.1021/nn304833s
10. Huang G, Jiang P, Zhang X, Zhou C, Zhou J, Huang Y, Yang P, Yang L, Tian X, Hao Y (2022) Efficient preparation and characterization of graphene based on ball milling. Diam Relat Mater 130:109438. https://doi.org/10.1016/j.diamond.2022.109438
11. Jian X, Liu S, Gao Y, Zhang W, He W, Mahmood A, Subramaniyam CM, Wang X, Mahmood N, Dou SX (2017) Facile synthesis of three-dimensional sandwiched MnO_2@GCs@MnO_2 hybrid nanostructured electrode for electrochemical capacitors. ACS Appl Mater Interfaces 9:18872–18882. https://doi.org/10.1021/acsami.7b04416
12. Jin X, Zhou W, Zhang S, Chen GZ (2007) Nanoscale microelectrochemical cells on carbon nanotubes. Small 3:1513–1517. https://doi.org/10.1002/smll.200700139
13. Lang X, Hirata A, Fujita T, Chen M (2011) Nanoporous metal/oxide hybrid electrodes for electrochemical supercapacitors. Nature Nanotech 6:232–236. https://doi.org/10.1038/nnano.2011.13
14. Lei Z, Shi F, Lu L (2012) Incorporation of MnO_2-coated carbon nanotubes between graphene sheets as supercapacitor electrode. ACS Appl Mater Interfaces 4:1058–1064. https://doi.org/10.1021/am2016848
15. Li W (2020) Review—an unpredictable hazard in lithium-ion batteries from transition metal ions: dissolution from cathodes, deposition on anodes and elimination strategies. J Electrochem Soc 167:090514. https://doi.org/10.1149/1945-7111/ab847f
16. Liu J, Zhang L, Wu HB, Lin J, Shen Z, Lou XWD (2014) High-performance flexible asymmetric supercapacitors based on a new graphene foam/carbon nanotube hybrid film. Energy Environ Sci 7:3709–3719. https://doi.org/10.1039/C4EE01475H
17 Ma X, Ma Y, Zhou J, Xiong S (2018) The recycling of spent power battery: economic benefits and policy suggestions. IOP Conf Ser Earth Environ Sci 159:012017. https://doi.org/10.1088/1755-1315/159/1/012017
18. Meng X, Lu L, Sun C (2018) Green synthesis of three-dimensional MnO_2/graphene hydrogel composites as a high-performance electrode material for supercapacitors. ACS Appl Mater Interfaces 10:16474–16481. https://doi.org/10.1021/acsami.8b02354
19. Natarajan S, Divya ML, Aravindan V (2022) Should we recycle the graphite from spent lithium-ion batteries? The untold story of graphite with the importance of recycling. J Energy Chem 71:351–369. https://doi.org/10.1016/j.jechem.2022.04.012
20. Natarajan S, Shanthana Lakshmi D, Bajaj HC, Srivastava DN (2015) Recovery and utilization of graphite and polymer materials from spent lithium-ion batteries for synthesizing polymer–graphite nanocomposite thin films. J Environ Chem Eng 3:2538–2545. https://doi.org/10.1016/j.jece.2015.09.011
21. Niu B, Xiao J, Xu Z (2022) Advances and challenges in anode graphite recycling from spent lithium-ion batteries. J Hazard Mater 439:129678. https://doi.org/10.1016/j.jhazmat.2022.129678
22. Perumal P, Mohapatra M, Mukherjee A, Basu S, Andersen SM (2022) Towering non-faradaic capacitive storage based on high quality reduced graphene oxide from spent graphite: direct approach and waste utilization. J Energy Storage 52:104989. https://doi.org/10.1016/j.est.2022.104989
23. Qu G, Li B, Wei Y (2023) A novel approach for the recovery and cyclic utilization of valuable metals by co-smelting spent lithium-ion batteries with copper slag. Chem Eng J 451:138897. https://doi.org/10.1016/j.cej.2022.138897
24. Shaheen I, Hussain I, Zahra T, Javed MS, Shah SSA, Khan K, Hanif MB, Assiri MA, Said Z, Arifeen WU, Akkinepally B, Zhang K (2023) Recent advancements in metal oxides for energy storage materials: design, classification, and electrodes configuration of supercapacitor. J Energy Storage 72:108719. https://doi.org/10.1016/j.est.2023.108719
25. Song Y, Liu T, Yao B, Li M, Kou T, Huang Z-H, Feng D-Y, Wang F, Tong Y, Liu X-X, Li Y (2017) Ostwald ripening improves rate capability of high mass loading manganese oxide for supercapacitors. ACS Energy Lett 2:1752–1759. https://doi.org/10.1021/acsenergylett.7b00405
26. Wang J, Guo X, Cui R, Huang H, Liu B, Li Y, Wang D, Zhao D, Dong J, Li S, Sun B (2020) MnO_2/porous carbon nanotube/MnO_2 nanocomposites for high-performance supercapacitor. ACS Appl Nano Mater 3:11152–11159. https://doi.org/10.1021/acsanm.0c02163
27. Wu L, Zhang FS, Zhang ZY, Zhang CC (2023) An environmentally friendly process for selective recovery of lithium and simultaneous synthesis of $LiFe_5O_8$ from spent $LiFePO_4$ battery by mechanochemical. J Clean Prod 396:136504. https://doi.org/10.1016/j.jclepro.2023.136504
28. Xu Y, Wang B, Wan Y, Sun Y, Wang W, Sun K, Yang L, Hu H, Wu M (2023) Understanding the process of lithium deposition on a graphite anode for better lithium-ion batteries. New Carbon Mater 38:678–693. https://doi.org/10.1016/S1872-5805(23)60747-4
29. Yan J, Fan Z, Wei T, Qie Z, Wang S, Zhang M (2008) Preparation and electrochemical characteristics of manganese dioxide/graphite nanoplatelet composites. Mater Sci Eng B 151:174–178. https://doi.org/10.1016/j.mseb.2008.05.018
30. Yan R, Li B, Zhou M, Li J, Xu Z (2023) Highly-efficient synthesis of heavy metal adsorbents by using spent lithium-ion battery anode graphite via one-step mechanochemistry process. Resour Conserv Recycl 190:106857. https://doi.org/10.1016/j.resconrec.2022.106857
31. Yan W, Kim JY, Xing W, Donavan KC, Ayvazian T, Penner RM (2012) Lithographically patterned gold/manganese dioxide core/shell nanowires for high capacity, high rate, and high cyclability hybrid electrical energy storage. Chem Mater 24:2382–2390. https://doi.org/10.1021/cm3011474
32. Yao B, Chandrasekaran S, Zhang J, Xiao W, Qian F, Zhu C, Duoss EB, Spadaccini CM, Worsley MA, Li Y (2019) Efficient 3D printed pseudocapacitive electrodes with ultrahigh MnO_2 loading. Joule 3:459–470. https://doi.org/10.1016/j.joule.2018.09.020
33. Yuan L, Lu X-H, Xiao X, Zhai T, Dai J, Zhang F, Hu B, Wang X, Gong L, Chen J, Hu C, Tong Y, Zhou J, Wang ZL (2012) Flexible Solid-state supercapacitors based on carbon nanoparticles/MnO_2 nanorods hybrid structure. ACS Nano 6:656–661. https://doi.org/10.1021/nn2041279
34. Zhang B, Zhang L, Wang Z, Gao Q (2024) An innovative wood derived carbon-carbon nanotubes-pyrolytic carbon composites with excellent electrical conductivity and thermal stability. J Mater Sci Technol 175:22–28. https://doi.org/10.1016/j.jmst.2023.07.040
35. Zhang G, Yuan X, Tay CY, He Y, Wang H, Duan C (2023) Selective recycling of lithium from spent lithium-ion batteries by carbothermal reduction combined with multistage leaching. Sep Purif Technol 314:123555. https://doi.org/10.1016/j.seppur.2023.123555
36. Zhang L, Yu X, Lv L, Zhu P, Zhou F, Li G, Sun R, Wong C. 2018. Ultrathin manganese dioxide nanosheets grown on mesoporous carbon hollow spheres for high performance asymmetrical supercapacitors. ACS Appl Energy Mater. acsaem.8b01022. https://doi.org/10.1021/acsaem.8b01022.
37. Zheng X, Zhu Z, Lin X, Zhang Y, He Y, Cao H, Sun Z (2018) A mini-review on metal recycling from spent lithium ion batteries. Engineering 4:361–370. https://doi.org/10.1016/j.eng.2018.05.018

Publisher's Note